Modeling electromechanical behaviors of soft conductive composites embedded with liquid metal fibers

Quang-Kha Nguyen, Pu Zhang[1]

Department of Mechanical Engineering, State University of New York at Binghamton, Binghamton, NY 13902, United States

Abstract:

Soft conductive materials are key components of soft electronics, sensors, actuators, and wearable devices. The electrical conductivity matrix or tensor of soft conductive materials is usually deformation-dependent, but there is a lack of constitutive modeling work on it. To fill this knowledge gap, we consider a soft conductive composite embedded with liquid metal fibers as an example. The difference between the material conductivity and spatial conductivity is clarified briefly. In addition, we devise two constitutive models for the deformation-dependent conductivity tensors. These two models are equivalent but in different formats, one using stretch ratios and the other using invariants. Besides the conductivity models, a transversely isotropic hyperelastic model is also presented to model the mechanical behaviors. These analytical models are fitted and validated using data from multiphysics computational modeling on representative volume elements. Note that the proposed models can also be used for other soft conductive materials as well as thermal conductivity modeling.

Keywords: Electromechanical behavior; Electrical conductivity; Soft conductive composite; Liquid metal

[1] Corresponding author. Email: pzhang@binghamton.edu

1 Introduction

Soft conductive composites usually consist of a compliant matrix embedded with solid or liquid conductive fillers [1,2]. They are essential components in emerging technological areas such as soft electronics, soft sensors and actuators, and soft robotics [1–4]. Among soft conductive composites, liquid metal composites [5,6] are among the most promising ones because of their high electrical conductivity, superb stretchability, and self-healing behavior. In the past few years, researchers have synthesized liquid metal composites with various micro-architectures [6,7], such as particulate composites [8,9], co-continuous composites [10,11], fiber composites [12], and hybrid fillers composites [13–15]. Among these, liquid metal fiber composites [12] have achieved high conductivity using a minimal amount of liquid metal, which not only reduces the material density but also the cost, showing high potential usage in soft electronics.

Even though various liquid metal composites have been fabricated and characterized experimentally, there are very few works regarding the theoretical and numerical modeling of their electromechanical behaviors. Researchers observed the deformation-dependent electrical conductivity [8,16] of liquid metal particulate composites, which deviates from the Pouillet's law [17] and depends on mechanical sintering. These early works [8,16] were merely experimental but inspired follow-up computational research. Cohen and Bhattacharya [18] were among pioneers who simulated the electromechanical behaviors of liquid metal particulate composites. They postulated that the conductance stems from the deformation-induced damage of the elastomer matrix and percolation of liquid metal droplets. In their simulation model, the liquid metal phase was treated as a hyperelastic solid with vanishing shear modulus. This approach is easy to implement and prevalent in following studies [17,19,20]. More detailed numerical study was carried out by Majidi et al. [17,20] to unravel the post-percolation behaviors by considering network topologies and the stochastic nature of percolation pathways. They found that the electromechanical behavior depends on the shape of percolation paths and the connectivity of liquid metal droplets with their neighbors. Regarding liquid metal co-continuous composites, Yao et al. [10] performed experimental testing and numerical simulation to uncover their electromechanical behaviors. They observed that the co-continuous composites have increased electrical conductivity upon stretching and attributed this phenomenon to the stretch-induced

alignment and elongation of the liquid metal phase. To date, we have not found other simulation works on the electrical conductivity of liquid metal composites.

A major knowledge gap is that there is a lack of constitutive modeling on the deformation-dependent conductivity tensors of soft conductive materials. Previous works on liquid metal composites [17,18,20,21] and carbon nanotube composites [22,23] were based on micromechanics simulation with explicit microstructures rather than macroscopic continuum modeling. Developing constitutive models of conductivity tensors will provide theories to describe and predict the electromechanical properties of soft conductive materials in general. This work aims at filling this knowledge gap by establishing a theoretical and computational framework and taking liquid metal fiber composites as examples. Meanwhile, the simulation results will also provide knowledge on the electromechanical behaviors of liquid metal fiber composites. Such simulation models and results will be useful to guide their design-optimization process towards better performance and more applications in soft electronics and multifunctional devices.

This work establishes a computational and theoretical framework to model liquid metal fiber composites with a random fiber network. The simulation is based on finite element modeling of representative volume elements (RVEs) with both mechanical and electrical analysis performed. Constitutive models of the electromechanical behaviors are devised for both the stress-strain and conductivity-strain relations. The novel contributions of this work are two constitutive models for the conductivity-strain relations, one using a stretch ratio approach and the other using invariants. Both models are equivalent and users can choose either one for their convenience. Besides the conductivity models, we also provide a transversely isotropic hyperelastic model to capture the mechanical behaviors of the composite. It is noted that the proposed models can also be used for soft conductive materials in general and for both electrical and thermal conductance modeling.

2 Computational modeling

2.1 The computational model

The major aim of the present work is to establish electromechanical constitutive models rather than simulating the fabricated composites directly [12]. Therefore, the computational model considered in this work is simplified from the experimental morphologies (Figure 1a) by assuming that liquid metal fibers are straight, continuous, and uniform (Figure 1b). For the simulation, three-

dimensional (3D) RVEs comprising both the soft matrix and the liquid metal fibers are created using the commercial finite element package ABAQUS (version 2020, Dassault Systemes). The fiber network is generated using a Centroidal Voronoi Tessellations (CVT) algorithm [24]. This algorithm generates more evenly distributed seed points than other similar algorithms. Once the seed points are sampled, fibers with a diameter d are randomly created and oriented at seed points to generate a fiber network (Figure 1b). Only one fiber is created for each seed point. The fiber generation process ceases once the given volume fraction of liquid metal V_f is reached. Instead of simulating a large RVE, we create three smaller RVEs (Figure 1c-e) to reduce computational cost. In our simulations, we found that the influence of network patterns on the stress-strain responses is marginal. The effective properties of the composite are the average of results from these three RVEs. The size of RVEs is 5 mm wide with the thickness ranging from 0.6 mm to 0.9 mm depending on volume fractions of liquid metal. Each RVE contains four layers of liquid metal fibers stacked along the thickness direction with the junction distance controlled at $0.75d$ as displayed in Figure 1f. In the finite element simulations, we assume that the fibers and the matrix are perfectly bonded. Composites with different volume fractions of liquid metal are generated by changing the fiber diameter. In this work, we investigate the composites with volume fractions of liquid metal as 5%, 10%, 15%, and 20%. The fiber diameters vary between 100μm to 250μm.

In order to extract the stress-strain and conductivity-strain relations, electromechanical simulations were performed on these RVEs using ABAQUS. The computational procedure consists of a mechanical analysis step followed by an electrical conductivity analysis step similarly reported in [25]. More specifically, the electrical conductivity analysis is performed on a pre-deformed RVE from the mechanical analysis step. Detailed analysis procedure is introduced below.

2.2 Mechanical analysis

The deformation of the composite RVE under an arbitrary loading condition is conducted first. The mechanical behaviors of the soft matrix and liquid metal are treated as nearly incompressible neo-Hookean solids. The soft matrix (Ecoflex 00-30, Smooth-On Inc.) is characterized by the initial shear modulus $\mu_{mat} = 21.6\times10^{-3}$ MPa [26] and bulk modulus $\kappa_{mat} = 500\mu_{mat}$. As reported in [18], large discrepancy between the soft matrix and liquid metal in mechanical properties leads to high computational cost and convergence difficulty. To overcome this issue, the initial shear

modulus and bulk modulus of liquid metal are approximated as $\mu_{\mathrm{LM}} = \mu_{\mathrm{mat}} / 20$ and $\kappa_{\mathrm{LM}} = \kappa_{\mathrm{mat}}$. The material properties of the soft matrix and liquid metal are summarized in Table 1. Next, the RVE is discretized by the hybrid element C3D4H. The mesh is refined until convergence is reached. Uniform displacement boundary conditions are imposed on the four lateral sides of the RVE, while the top and bottom surfaces are free. Average true stress (Cauchy stress) and true strain (spatial Hencky strain) are extracted from the simulation results for constitutive modeling usage. In addition, the displacement fields of each frame are exported for the electrical conductivity analysis step.

2.3 Electrical conductivity analysis

To evaluate the effective electrical conductivity of the composite at different stretching levels, an isothermal steady-state linear electrical conductivity analysis (coupled thermal-electrical step in ABAQUS) is performed on the deformed solid mesh imported from the mechanical analysis step. To ensure high accuracy of the results at the highly deformed configuration, a 10-node quadratic coupled thermal-electrical tetrahedron element DC3D10E is employed in the electrical conductivity analysis. Specifically, for each element, displacements of the six edge nodes are interpolated from that of the four corner nodes. Moreover, the soft matrix is treated as an electrical insulator $\sigma^{\mathrm{E}}_{\mathrm{mat}} \approx 0$ whereas the liquid metal is a conductor with $\sigma^{\mathrm{E}}_{\mathrm{LM}} = 3400$ S/mm.

As shown in Figure 2, the electrical conductivity equation can be formulated either in the reference configuration Ω_R or the current configuration Ω. In the current configuration Ω, the current density $\mathbf{j}$ is described by the spatial Ohm's law

$$\mathbf{j} = \boldsymbol{\sigma}^{\mathrm{E}}\mathbf{E} \tag{1}$$

where $\boldsymbol{\sigma}^{\mathrm{E}}$ is the spatial conductivity tensor, $\mathbf{E} = -\mathrm{grad}\,\phi$ is the electrical field intensity vector, and ϕ is the spatial electrical potential. Normally, the spatial conductivity tensor $\boldsymbol{\sigma}^{\mathrm{E}}$ is employed for simulation and applications given its clear physical meaning.

Electrical boundary conditions on RVEs are key to the simulation. Note that the electrical conductivity of the composite is independent to the boundary conditions. However, we should apply special electrical boundary conditions to obtain the electrical potentials more easily. In particular, we specify a linear potential function on all the surface nodes as

$$\phi(x, y) = -(E_x x + E_y y) \text{ for all surface nodes} \tag{2}$$

Two sets of electrical boundary conditions are applied by specifying either E_x or E_y along the two in-plane directions, respectively. The effective current density of the RVE is obtained by the volume-average of the element current density $\mathbf{j}_e$ of all elements, as

$$\langle \mathbf{j} \rangle = \frac{1}{V} \sum_e \mathbf{j}_e V_e \tag{3}$$

where V_e denotes element volume and V is the total volume. Finally, the spatial conductivity tensor is obtained as [27]

$$\sigma_{ij}^{\mathrm{E}} = \frac{\langle j_i \rangle}{E_j} \tag{4}$$

where the current density $\langle j_i \rangle$ is from Eq. (3) and the electrical potential E_j is provided in the applied boundary conditions. By simulating the spatial conductivity of each deformed frame from the mechanical analysis step, we can obtain the conductivity-strain relations.

3 Electromechanical constitutive modeling

3.1 Hyperelastic stress-strain relation

The soft composite with randomly oriented fibers can be considered as transversely isotropic. The mechanical properties are symmetric about the Z axis with the X-Y plane as the plane of isotropy defined in Figure 1. We identify the direction normal to the isotropy plane by a unit vector $\mathbf{N}$ and $\mathbf{n}$ in the reference configuration and current configuration, respectively. The composite is modeled as a transversely isotropic hyperelastic material. Such a material can be characterized by a strain energy density function W that depends on strain invariants and the structural tensor $\mathbf{N} \otimes \mathbf{N}$. There are many choices of strain energy density functions [28]. Herein we adopt a strain energy density function in the following form [28]

$$W(I_1, I_4) = \frac{\bar{\mu}}{2}(I_1 - 3) + \frac{\tilde{\mu}}{2}(\quad\quad - 1)^2 \tag{5}$$

where the first term represents the isotropic part using a neo-Hookean model, the second term considers the anisotropic energy contribution, $\bar{\mu}$ and $\tilde{\mu}$ are elastic constants. The invariants I_1, I_3, and I_4 are defined as

$$I_1 = \mathrm{tr}\mathbf{C},\ I_3 = \det\mathbf{C} = J^2,\ I_4 = \mathbf{C}:(\mathbf{N}\otimes\mathbf{N}) \tag{6}$$

where $\mathbf{C} = \mathbf{F}^{\mathrm{T}}\mathbf{F}$ is the right Cauchy-Green tensor, $\mathbf{F}$ is the deformation gradient and $J = \det\mathbf{F}$.

In this work, we consider the composite as incompressible with $J = 1$. The second Piola-Kirchhoff stress $\mathbf{S}$ (see Figure 2) of an incompressible hyperelastic material is obtained [29] by differentiating the strain energy function with respect to $\mathbf{C}$ as

$$\begin{aligned}\mathbf{S} &= 2\frac{\partial W(I_1, I_4)}{\partial \mathbf{C}} - \frac{\partial\left[p(I_3 - 1)\right]}{\partial \mathbf{C}} \\ &= -p\mathbf{C}^{-1} + \bar{\mu}\mathbf{I} + \tilde{\mu}\left(\quad\right)\mathbf{N}\otimes\mathbf{N}\end{aligned} \tag{7}$$

where p is a Lagrange multiplier representing the hydrostatic pressure, and $\mathbf{I}$ is the identity tensor in the 3D space.

Accordingly, the corresponding Cauchy stress (see Figure 2) $\boldsymbol{\sigma} = J^{-1}\mathbf{F}\mathbf{S}\mathbf{F}^{\mathrm{T}}$ is given by

$$\boldsymbol{\sigma} = -p\mathbf{I} + \bar{\mu}\mathbf{b} + \tilde{\mu}\left(\quad\right)I_4\mathbf{n}\otimes\mathbf{n} \tag{8}$$

in which $\mathbf{b} = \mathbf{F}\mathbf{F}^{\mathrm{T}}$ is the left Cauchy-Green tensor, and recall that $\mathbf{n} = \mathbf{F}\mathbf{N}/|\mathbf{F}\mathbf{N}|$ is the unit vector along the thickness direction in the current configuration.

3.2 Conductivity-strain relation

Soft conductive composites are usually used as thin films and only the in-plane conductivity is of interest. Hence, the liquid metal composite considered here is electrically insulated along the thickness direction. For the sake of convenience, the spatial conductivity tensor $\boldsymbol{\sigma}^{\mathrm{E}}$ of the composite is defined in the two-dimensional (2D) space, and only the in-plane components are considered. Under in-plane uni-/biaxial loading, the spatial conductivity becomes orthotropic due to the stretch-induced anisotropy. Based on the simulation results, we aim to develop analytical expressions for the conductivity-strain relations. Two equivalent models are proposed below using stretch ratios (model I) and invariants (model II), respectively.

Conductivity model I. Given that the material is isotropic in-plane, the spatial conductivity tensor $\boldsymbol{\sigma}^{\mathrm{E}}$ in the current configuration is coaxial to the left Cauchy Green tensor **b**. Therefore, we can express the spatial conductivity tensor in the principal directions, as

$$\boldsymbol{\sigma}^{\mathrm{E}} = \sigma_{11}^{\mathrm{E}} \mathbf{n}_1 \otimes \mathbf{n}_1 + \sigma_{22}^{\mathrm{E}} \mathbf{n}_2 \otimes \mathbf{n}_2 \tag{9}$$

where $\mathbf{n}_1$ and $\mathbf{n}_2$ are the in-plane principal directions of $\mathbf{b}$, and 1 and 2 indicate the two principal axes. The principal conductivity values σ_{11}^{E} and σ_{22}^{E} are unknown functions in terms of the stretch ratios λ_1 and λ_2. In this work, we propose the following exponential functions for them, as

$$\begin{aligned} \sigma_{11}^{\mathrm{E}}(\lambda_1, \lambda_2) &= a_0 + a_1 e^{b_1 \lambda_1} + a_2 e^{b_2 \lambda_2} + a_{12} e^{b_{12}/(\lambda_1 \lambda_2)}, \\ \sigma_{22}^{\mathrm{E}}(\lambda_1, \lambda_2) &= a_0 + a_1 e^{b_1 \lambda_2} + a_2 e^{b_2 \lambda_1} + a_{12} e^{b_{12}/(\lambda_2 \lambda_1)} \end{aligned} \tag{10}$$

in which $a_0, a_1, b_1, a_2, b_2, a_{12}, b_{12}$ are seven model parameters to be calibrated. Note that Eq. (10) must satisfy a hidden symmetry condition $\sigma_{11}^{\mathrm{E}}(\lambda_1, \lambda_2) = \sigma_{22}^{\mathrm{E}}(\lambda_2, \lambda_1)$ to make the model self-consistent.

Conductivity model II. Additionally, the spatial conductivity $\boldsymbol{\sigma}^{\mathrm{E}}$ can be represented in terms of invariants. Following the representation theory of tensor functions in the 2D space [30], the spatial conductivity tensor can be expressed in this explicit form

$$\boldsymbol{\sigma}^{\mathrm{E}} = \alpha_0 \tilde{\quad} \quad \tilde{} \tag{11}$$

where $\tilde{}$ and $\tilde{}$ are the left Cauchy-Green tensor and identity tensor in the 2D space, which serve as the integrity bases, as

$$\tilde{} \quad \begin{bmatrix} & \\ b_{21} & b_{22} \end{bmatrix} \quad \tilde{} \quad \begin{bmatrix} & \\ 0 & 1 \end{bmatrix} \tag{12}$$

Here we use the tilde sign to indicate symbols in the 2D space. In addition, the functional bases $\alpha_0(\tilde{} \ \tilde{}$ and $\alpha_1(\tilde{} \ \tilde{}$ in Eq. (11) are unknown functions of the invariants $\tilde{} \quad \tilde{}$ and $\tilde{} \quad \tilde{}$. In this work, we propose the following power laws for the functional bases as

$$\begin{aligned} \alpha_0(\tilde{} \ \tilde{} \quad \tilde{} \ \tilde{} \\ \alpha_1(\tilde{} \ \tilde{} \quad \tilde{} \ \tilde{} \end{aligned} \tag{13}$$

where $\bar{a}_0, \bar{b}_0, \bar{c}_0, \bar{a}_1, \bar{b}_1, \bar{c}_1$ are six model parameters to be calibrated from simulation data.

We have three remarks for the two conductivity models in Eq. (9) and Eq. (11).

- The two models are equivalent. Model I is convenient for experimental calibration while the model II is convenient for simulation implementation. The model I has a clearer physical meaning.
- The two models in Eq. (10) and Eq. (13) are phenomenological so that the specific function forms can be modified. In theory, one can use other functions as well, e.g., exponential, power, logarithmic, and polynomial functions. We choose the functions in Eq. (10) and Eq. (13) mainly by considering their accuracy and simplicity. The discovery of these specific expressions takes a lengthy trial-and-error process.
- The model parameters are calibrated by using a least square optimization method from the simulation data. The optimization may result in multiple parameter sets depending on the initial guess values**.**

3.3 Remarks on conductivity in the reference configuration

For continuum modeling, physical quantities and governing equations can be formulated in either the reference or current configuration. As shown in Figure 2, one can also formulate Eq. (1) as a material Ohm's law in the reference configuration as

$$\mathbf{j}_R = \boldsymbol{\sigma}_R^{\mathrm{E}} \mathbf{E}_R \tag{14}$$

where the subscript R indicates the reference configuration, and $\boldsymbol{\sigma}_R^{\mathrm{E}}$ is the material conductivity tensor (oppose to the spatial conductivity tensor $\boldsymbol{\sigma}^{\mathrm{E}}$). This alternative version of Ohm's law is not commonly used; but it is useful for the constitutive modeling purpose. The two Ohm's laws can be correlated by tensor transformation. The transformation relations [31] are given as

$$\begin{aligned} \mathbf{j} &= J^{-1}\mathbf{F}\mathbf{j}_R, \\ \mathbf{E} &= \mathbf{F}^{-\mathrm{T}}\mathbf{E}_R, \\ \boldsymbol{\sigma}^{\mathrm{E}} &= J^{-1}\mathbf{F}\boldsymbol{\sigma}_R^{\mathrm{E}}\mathbf{F}^{\mathrm{T}} \end{aligned} \tag{15}$$

Certainly, the two Ohm's laws and two conductivity tensors are identical for small deformation.

The two conductivity models in Eq. (9) and Eq. (11) are formulated in the current configuration. According to Eq. (15), they can be pulled back to the reference configuration as

$$\boldsymbol{\sigma}_R^{\mathrm{E}} = J\mathbf{F}^{-1}\boldsymbol{\sigma}^{\mathrm{E}}\mathbf{F}^{-\mathrm{T}} \tag{16}$$

More explicitly, the material conductivity tensor corresponding to Eq. (9) and (11) are respectively,

$$\boldsymbol{\sigma}_R^{\mathrm{E}} = \frac{J\sigma_{11}^{\mathrm{E}}}{\lambda_1^2}\mathbf{N}_1 \otimes \mathbf{N}_1 + \frac{J\sigma_{22}^{\mathrm{E}}}{\lambda_2^2}\mathbf{N}_2 \otimes \mathbf{N}_2 \tag{17}$$

$$\boldsymbol{\sigma}_R^{\mathrm{E}} = J\alpha_0(\tilde{\quad} \qquad \tilde{} \tag{18}$$

where $J = 1$ for incompressible materials, ($\tilde{}$ is the in-plane right Cauchy-Green tensor, $\mathbf{N}_1$ and $\mathbf{N}_2$ are the principal directions of ($\tilde{}$. Usually, the soft electronics applications prefer strain-insensitive conductivity [12,17], which requires the material conductivity tensor $\boldsymbol{\sigma}_R^{\mathrm{E}} = const.$ and the spatial conductivity tensor $\boldsymbol{\sigma}^{\mathrm{E}} \propto \tilde{}$. Designing and fabricating soft conductors that exhibit such a special feature are significant future research tasks.

4 Results and discussions

We begin by investigating the mechanical behaviors of the liquid metal fiber composites. The three RVEs in Figure 1 are simulated and their average stress-strain relations are obtained. The hyperelastic material constants $\bar{\mu}$ and $\tilde{}$ in Eq. (8) are calibrated based on the simulation results. Herein, we consider three different loading scenarios that include uniaxial, biaxial with ratio $k = \lambda_x / \lambda_y$, and equibiaxial ($k = 1$). Figure 3 displays the stress-strain curves of the composites with different volume fractions of liquid metal (V_f = 5-20%). The true strain (ϵ) is used in this figure. Figure 3a shows the stress-strain curves under uniaxial loading. The inclusion of liquid metal softens the composite with evidence that the stiffness decreases. Note that we have ignored the oxide layer of the liquid metal phase in this work. The stiffness the oxide plays an effect only when the liquid metal inclusions are sub-micron [32]. Besides the uniaxial data, the results for equibiaxial and biaxial loading are also shown in Figure 3b and Figure 3c-d, respectively. Overall, the proposed hyperelastic model in (5) and (8) fits well to the finite element simulation data. The two material constants $\bar{\mu}$ and $\tilde{}$ in the hyperelastic model are provided in Table 2. With higher volume fraction of liquid metal, both the isotropic material constant $\bar{\mu}$ and anisotropic material constant $\tilde{}$ decrease because that the strain energy contribution from the liquid metal phase is lower than that in the matrix. In general, the isotropic part is around one order of magnitude greater than the anisotropic part, indicating that this liquid metal fiber composite is weakly anisotropic. Moreover, the constant $\tilde{}$ approaches zero at the volume fraction of 20%.

In the following, we study the electromechanical behaviors of the composites. Note that we focus on the spatial conductivity $\boldsymbol{\sigma}^{\mathrm{E}}$ here. At first, we examine the effect of non-affine deformation on the spatial conductivity of the composite. The non-affine (i.e., non-uniform) deformation is induced by the stiffness mismatch between the matrix and fibers. If they have identical hyperelastic parameters, the overall deformation of the composite is affine; but in reality, the deformation is non-affine. It was known that such non-affinity has influence on mechanical behaviors of network materials [33], but there is no research on electromechanical behaviors. In order to elucidate this effect, we perform two sets of simulations: one is affine by assigning the fibers with the same hyperelastic properties as the matrix, and the other is non-affine by assigning different hyperelastic properties. Figure 4a presents the spatial conductivity versus stretch ratio under different loading conditions. It is observed that the spatial conductivity σ_{xx}^{E} in the current configuration increases with the stretch. Actually, the material conductivity $\sigma_{Rxx}^{\mathrm{E}} = \sigma_{xx}^{\mathrm{E}} / \lambda_x^2$ in the reference configuration derived from Eq. (17) decreases meanwhile, which is known as the piezoresistance effect. By comparing the affine and non-affine results, there is discrepancy between the conductivities under different loading conditions. In all scenarios here, the non-affinity increases the spatial conductivity. This phenomenon can be explained by comparing the microstructure changes under affine and non-affine deformation illustrated in Figure 4b. In Figure 4b, the liquid metal fibers are wider under non-affine deformation because they are softer and stretched more severely than the matrix, which facilitates local current flow and increases the overall spatial conductivity. There is another effect called junction effect here, which is more complicated. Take the equibiaxial case as an example, the network geometry is unaltered under stretch and so the spatial conductivity of the composite is expected to be constant. Nevertheless, we still observe a slight increase of the spatial conductivity, which is attributed to the electrical current leakage at junctions that improves the conductivity. In general, the spatial conductivity of the liquid metal fiber composites is related to the deformation mode, non-affinity, and junctions. On the other hand, the material conductivity can be transformed using Eqs. (16) and (17) accordingly and will not be discussed here.

Next, we present the spatial conductivity of the composite under different stretch deformation. In order to visualize the spatial conductivity response surfaces under arbitrary deformation, we plot the spatial conductivity as a function of stretch ratios λ_x and λ_y. Figure 5 shows the 3D

surface of the spatial conductivity σ_{xx}^{E} under uniaxial and biaxial loading scenarios with different ratios *k*. The data are obtained from simulation. As shown in Figure 5, the spatial conductivity depends on the stretch mode. Different stretch ratios can either increase or decrease the spatial conductivity of the composite along different directions, depending on how they change the fiber orientations and the size of the junctions.

The spatial conductivity data in Figure 5 are used to fit the conductivity model I with parameters provided in Table 3. Note that the principal stretch ratios λ_1 and λ_2 are used in model I. For the case $\lambda_x \geq \lambda_y$, we have $\lambda_1 = \lambda_x$ and $\lambda_2 = \lambda_y$; otherwise, we have $\lambda_1 = \lambda_y$ and $\lambda_2 = \lambda_x$. To show the influence of stretch deformation on the spatial conductivity clearer, some data in Figure 5 are adapted and replotted in Figure 6. The principal spatial conductivity σ_{11}^{E} and σ_{22}^{E} are plotted versus the principal stretch ratio λ_1 in Figure 6. Overall, the proposed conductivity model I fits well with the simulation data for all volume fractions and deformation modes considered here, which validates the proposed constitutive model. The spatial conductivity σ_{11}^{E} is observed to increase with a greater ratio *k*. In contrary, the spatial conductivity σ_{22}^{E} decreases with a greater ratio *k*. This is because that a greater *k* ratio means that the composite is more stretched along the 1-axis than the 2-axis, which makes the fibers aligned more toward the 1-axis. Specifically, for uniaxial stretching cases, the longitudinal spatial conductivity σ_{11}^{E} increases while the transverse spatial conductivity σ_{22}^{E} decreases under uniaxial stretch loading. We have shown the data with different volume fractions of liquid metal in Figures 5 and 6, and the general trends are consistent.

Finally, as introduced in Section 3.2, the spatial conductivity can also be expressed in terms of strain invariants $\tilde{.}$ and $\tilde{.}$. Figure 7 visualizes the 3D surfaces of spatial conductivity σ_{11}^{E} and σ_{22}^{E} in the invariant space with data adapted from Figure 5. These data are used to fit the proposed conductivity model II with optimal parameters given in Table 4. In addition, some data are also adapted and replotted in Figure 8 to show the comparison clearer. Overall, the results obtained from the model II show almost perfect agreement with the simulation results, which demonstrates the effectiveness of the proposed model. We recognize that the spatial conductivity surfaces in the

invariant space do not have very intuitive physical meaning. This type of constitutive model is merely convenient to perform simulations rather than to interpret physics.

5 Conclusions

Soft conductors are essential components in emerging technologies such as soft electronics and robotics. However, there is a lack of systematic constitutive modeling research on soft conductors. For soft conductors, there exist two Ohm's laws in the reference and current configurations. Accordingly, we can define a material conductivity tensor in the reference configuration and a spatial conductivity tensor in the current configuration. We need to develop not only the stress-strain relations but also the conductivity-strain relations for constitutive modeling of soft conductors. In this work, we consider liquid metal fiber composites as an example and studied their electromechanical behaviors. A hyperelastic model is established for their stress-strain relations. Meanwhile, two models are proposed for their conductivity-strain relations, one using stretch ratios and the other using invariants. These electromechanical constitutive laws are fitted using data from finite element simulation with different loading scenarios. We have found that the proposed constitutive models can describe the electromechanical behaviors of liquid metal fiber composites pretty well. Moreover, it is found that the composite's conductivity either increases or decreases depending on the microstructure change, loading conditions, orientations, and configurations. For example, under uniaxial stretch, the longitudinal spatial conductivity increases while the transverse spatial conductivity decreases. In addition, we found that the intrinsic non-affine deformation and junction effect of the liquid metal fiber composites are found to improve their spatial conductivity. We expect that the proposed constitutive models can be used to describe the electromechanical behaviors of other soft conductors as well as thermal conductivity modeling.

6 Acknowledgments

The authors want to thank the funding support from National Science Foundation (CMMI-2143297, CMMI-2244952) for this work.

References

[1] Choi, S., Han, S. I., Kim, D., Hyeon, T., and Kim, D.-H., 2019, "High-Performance Stretchable Conductive Nanocomposites: Materials, Processes, and Device Applications," Chem. Soc. Rev., **48**(6), pp. 1566–1595.

[2] Yun, G., Tang, S.-Y., Lu, H., Zhang, S., Dickey, M. D., and Li, W., 2021, "Hybrid-Filler Stretchable Conductive Composites: From Fabrication to Application," Small Science, **1**(6), p. 2000080.

[3] Gui, Q., He, Y., and Wang, Y., 2021, "Soft Electronics Based on Liquid Conductors," Adv. Electron. Mater., **7**(1), p. 2000780.

[4] Won, P., Jeong, S., Majidi, C., and Ko, S. H., 2021, "Recent Advances in Liquid-Metal-Based Wearable Electronics and Materials," iScience, **24**(7), p. 102698.

[5] Chen, S., Wang, H.-Z., Zhao, R.-Q., Rao, W., and Liu, J., 2020, "Liquid Metal Composites," Matter, **2**(6), pp. 1446–1480.

[6] Style, R. W., Tutika, R., Kim, J. Y., and Bartlett, M. D., 2021, "Solid–Liquid Composites for Soft Multifunctional Materials," Adv. Funct. Mater., **31**(1), p. 2005804.

[7] Guymon, G. G., and Malakooti, M. H., 2022, "Multifunctional Liquid Metal Polymer Composites," Journal of Polymer Science, **60**(8), pp. 1300–1327.

[8] Fassler, A., and Majidi, C., 2015, "Liquid-Phase Metal Inclusions for a Conductive Polymer Composite," Advanced Materials, **27**(11), pp. 1928–1932.

[9] Tutika, R., Kmiec, S., Haque, A. B. M. T., Martin, S. W., and Bartlett, M. D., 2019, "Liquid Metal–Elastomer Soft Composites with Independently Controllable and Highly Tunable Droplet Size and Volume Loading," ACS Appl. Mater. Interfaces, **11**(19), pp. 17873–17883.

[10] Yao, B., Hong, W., Chen, T., Han, Z., Xu, X., Hu, R., Hao, J., Li, C., Li, H., Perini, S. E., Lanagan, M. T., Zhang, S., Wang, Q., and Wang, H., 2020, "Highly Stretchable Polymer Composite with Strain-Enhanced Electromagnetic Interference Shielding Effectiveness," Advanced Materials, **32**(14), p. 1907499.

[11] Liang, S., Li, Y., Chen, Y., Yang, J., Zhu, T., Zhu, D., He, C., Liu, Y., Handschuh-Wang, S., and Zhou, X., 2017, "Liquid Metal Sponges for Mechanically Durable, All-Soft, Electrical Conductors," J. Mater. Chem. C, **5**(7), pp. 1586–1590.

[12] Ma, J., Liu, Z., Nguyen, Q.-K., and Zhang, P., 2023, "Lightweight Soft Conductive Composites Embedded with Liquid Metal Fiber Networks," Adv. Funct. Mater., p. 2308128.

[13] Saborio, M. G., Cai, S., Tang, J., Ghasemian, M. B., Mayyas, M., Han, J., Christoe, M. J., Peng, S., Koshy, P., Esrafilzadeh, D., Jalili, R., Wang, C. H., and Kalantar-Zadeh, K., 2020, "Liquid Metal Droplet and Graphene Co-Fillers for Electrically Conductive Flexible Composites," Small, **16**(12), p. 1903753.

[14] Mohammadi Nasab, A., Sharifi, S., Chen, S., Jiao, Y., and Shan, W., 2021, "Robust Three-Component Elastomer–Particle–Fiber Composites with Tunable Properties for Soft Robotics," Advanced Intelligent Systems, **3**(2), p. 2000166.

[15] Parida, K., Thangavel, G., Cai, G., Zhou, X., Park, S., Xiong, J., and Lee, P. S., 2019, "Extremely Stretchable and Self-Healing Conductor Based on Thermoplastic Elastomer for All-Three-Dimensional Printed Triboelectric Nanogenerator," Nat Commun, **10**(1), p. 2158.

[16] Thrasher, C. J., Farrell, Z. J., Morris, N. J., Willey, C. L., and Tabor, C. E., 2019, "Mechanoresponsive Polymerized Liquid Metal Networks," Advanced Materials, **31**(40), p. 1903864.

[17] Zolfaghari, N., Khandagale, P., Ford, M. J., Dayal, K., and Majidi, C., 2020, "Network Topologies Dictate Electromechanical Coupling in Liquid Metal–Elastomer Composites," Soft Matter, **16**(38), pp. 8818–8825.

[18] Cohen, N., and Bhattacharya, K., 2019, "A Numerical Study of the Electromechanical Response of Liquid Metal Embedded Elastomers," International Journal of Non-Linear Mechanics, **108**, pp. 81–86.

[19] Nguyen, Q.-K., Ma, J., and Zhang, P., 2023, "Liquid Metal-Filled Phase Change Composites with Tunable Stiffness: Computational Modeling and Experiment," Mechanics of Materials, **183**, p. 104702.

[20] Zhao, Y., Khandagale, P., and Majidi, C., 2021, "Modeling Electromechanical Coupling of Liquid Metal Embedded Elastomers While Accounting Stochasticity in 3D Percolation," Extreme Mechanics Letters, **48**, p. 101443.

[21] Yao, B., Hong, W., Chen, T., Han, Z., Xu, X., Hu, R., Hao, J., Li, C., Li, H., Perini, S. E., Lanagan, M. T., Zhang, S., Wang, Q., and Wang, H., 2020, "Highly Stretchable Polymer Composite with Strain-Enhanced Electromagnetic Interference Shielding Effectiveness," Adv. Mater., **32**(14), p. 1907499.

[22] Jung, S., Choi, H. W., Mocanu, F. C., Shin, D.-W., Chowdhury, M. F., Han, S. D., Suh, Y.-H., Cho, Y., Lee, H., Fan, X., Bang, S. Y., Zhan, S., Yang, J., Hou, B., Chun, Y. T., Lee, S., Occhipinti, L. G., and Kim, J. M., 2019, "Modeling Electrical Percolation to Optimize the Electromechanical Properties of CNT/Polymer Composites in Highly Stretchable Fiber Strain Sensors," Sci Rep, **9**(1), p. 20376.

[23] Fu, X., Al-Jumaily, A. M., Ramos, M., and Chen, Y.-F., 2018, "Comprehensive Analysis on the Electrical Behavior of Highly Stretchable Carbon Nanotubes/Polymer Composite through Numerical Simulation," J. Mater. Res., **33**(20), pp. 3398–3407.

[24] Du, Q., Faber, V., and Gunzburger, M., 1999, "Centroidal Voronoi Tessellations: Applications and Algorithms," SIAM Rev., **41**(4), pp. 637–676.

[25] Overvelde, J. T. B., Mengüç, Y., Polygerinos, P., Wang, Y., Wang, Z., Walsh, C. J., Wood, R. J., and Bertoldi, K., 2014, "Mechanical and Electrical Numerical Analysis of Soft Liquid-Embedded Deformation Sensors Analysis," Extreme Mechanics Letters, **1**, pp. 42–46.

[26] Overvelde, J. T. B., Dykstra, D. M. J., de Rooij, R., Weaver, J., and Bertoldi, K., 2016, "Tensile Instability in a Thick Elastic Body," Phys. Rev. Lett., **117**(9), p. 094301.

[27] Kim, D.-W., Lim, J. H., and Yu, J., 2019, "Efficient Prediction of the Electrical Conductivity and Percolation Threshold of Nanocomposite Containing Spherical Particles with Three-Dimensional Random Representative Volume Elements by Random Filler Removal," Composites Part B: Engineering, **168**, pp. 387–397.

[28] Chagnon, G., Rebouah, M., and Favier, D., 2015, "Hyperelastic Energy Densities for Soft Biological Tissues: A Review," J Elast, **120**(2), pp. 129–160.

[29] Holzapfel, G. A., 2000, *Nonlinear Solid Mechanics. A Continuum Approach for Engineering*, Wiley, Chichester.

[30] Zheng, Q.-S., 1994, "Theory of Representations for Tensor Functions—A Unified Invariant Approach to Constitutive Equations," Applied Mechanics Reviews, **47**(11), pp. 545–587.

[31] Wang, Y., and Wright, N. T., 2005, "A Relationship between Thermal Diffusivity and Finite Deformation in Polymers," Int J Thermophys, **26**(6), pp. 1849–1859.

[32] Malakooti, M. H., Bockstaller, M. R., Matyjaszewski, K., and Majidi, C., 2020, "Liquid Metal Nanocomposites," Nanoscale Adv., **2**(7), pp. 2668–2677.

[33] Picu, R. C., 2011, "Mechanics of Random Fiber Networks—a Review," Soft Matter, **7**(15), p. 6768.

Table 1. Material properties used for the simulation.

	Shear modulus (MPa)	Bulk modulus (MPa)	Conductivity (S/mm)
Soft matrix	$\mu_{\text{mat}} = 21.6\times10^{-3}$	$\kappa_{\text{mat}} = 10.8$	$\sigma^{\text{E}}_{\text{mat}} \approx 0$
Liquid metal	$\mu_{\text{LM}} = 1.08\times10^{-3}$	$\kappa_{\text{LM}} = 10.8$	$\sigma^{\text{E}}_{\text{LM}} = 3400$

Table 2. Model parameters for the hyperelastic stress-strain relations of the composites.

V_f (%)	$\bar{\mu}$ (MPa)	$\tilde{\mu}$ (MPa)
5	19.936×10^{-3}	5.351×10^{-3}
10	18.491×10^{-3}	3.174×10^{-3}
15	17.043×10^{-3}	1.140×10^{-3}
20	15.561×10^{-3}	0.015×10^{-3}

Table 3. Model parameters for the conductivity-strain relations using model I.

V_f (%)	a_0 (S/mm)	a_1 (S/mm)	b_1	a_2 (S/mm)	b_2	a_{12} (S/mm)	b_{12}
5	72.43	-104.10	-0.5311	98.69	-0.2805	50.82	-35.12
10	176.20	-230.90	-0.5311	185.70	-0.2805	117.90	-35.12
15	311.80	-366.80	-0.5311	237.20	-0.2805	187.60	-35.12
20	499.90	-514.10	-0.5311	240.50	-0.2805	215.00	-35.12

Table 4. Model parameters for the conductivity-strain relations using model II.

V_f (%)	$\bar{a}_0$ (S/mm)	$\bar{b}_0$	$\bar{c}_0$	$\bar{a}_1$ (S/mm)	$\bar{b}_1$	$\bar{c}_1$
5	59.44	-0.4513	0.2830	72.193	-0.7442	-0.1419
10	125.66	-0.4184	0.2885	151.05	-0.7470	-0.1455
15	199.63	-0.3878	0.2909	221.63	-0.7394	-0.1592
20	294.89	-0.3324	0.2701	277.71	-0.7214	-0.1809

Figure Captions

Figure 1. (a) Optical microscopy of a liquid metal fiber composite (image is adapted from [12] with permission); (b) A randomly oriented liquid metal fiber network constructed using the CVT algorithm; (c)-(e) Three different RVEs of the liquid metal fiber composites; and (f) Junction distance illustration.

Figure 2. Continuum modeling of the electromechanical behavior of a soft conductor. The stress-strain relation and conductivity-strain relation can be formulated either in the reference configuration Ω_R or the current configuration Ω. There are two Ohm's laws considering the two configurations. Accordingly, we can define a material conductivity tensor $\boldsymbol{\sigma}_R^{\mathrm{E}}$ and a spatial conductivity tensor $\boldsymbol{\sigma}^{\mathrm{E}}$.

Figure 3. Stress-strain relations of the composites under different loading scenario: (a) Uniaxial loading, σ_{xx}; (b) Equibiaxial loading, $\sigma_{xx}=\sigma_{yy}$; (c) Biaxial loading, σ_{xx}; and (d) Biaxial loading, σ_{yy}.

Figure 4. Conductivity-strain responses of the composite with affine and non-affine simulation for the case $V_{\mathrm{f}}=10\%$: (a) Electrical conductivity; (b) Electrical current density for $\lambda_x=4$.

Figure 5. 3D surface plot of conductivity-strain relations under arbitrary biaxial loadings obtained from simulation: (a) $V_{\mathrm{f}}=5\%$; (b) $V_{\mathrm{f}}=10\%$; (c) $V_{\mathrm{f}}=15\%$; and (d) $V_{\mathrm{f}}=20\%$.

Figure 6. Conductivity-strain relations in the principal coordinate system from simulation and the conductivity model I. (a-d) σ_{11}^{E}; and (e-h) σ_{22}^{E}. The principal coordinate system is used here.

Figure 7. 3D surface plot of conductivity-strain relations in the invariant space under arbitrary biaxial loadings obtained from simulation: (a-d) σ_{11}^{E}; and (e-h) σ_{22}^{E}. The principal coordinate system is used here. The data are adapted from Figure 5.

Figure 8. Conductivity-strain relations in the invariant space from simulation and the conductivity model II. (a-d) σ_{11}^{E}; and (e-h) σ_{22}^{E}.

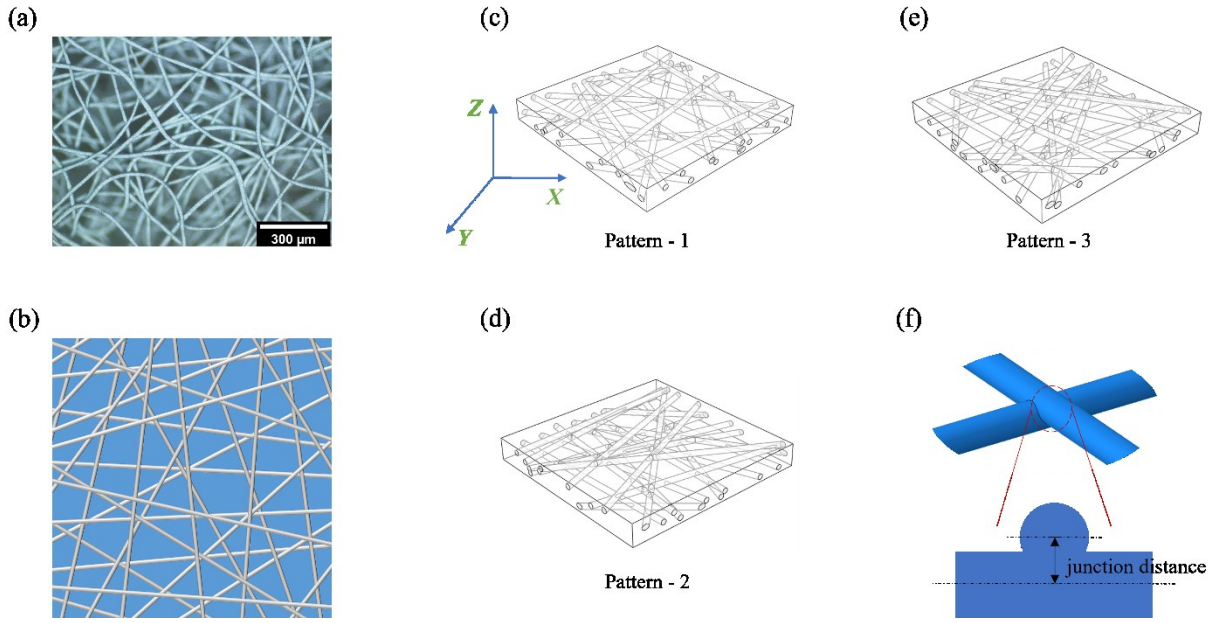

Figure 1. (a) Optical microscopy of a liquid metal fiber composite (image is adapted from [12] with permission); (b) A randomly oriented liquid metal fiber network constructed using the CVT algorithm; (c)-(e) Three different RVEs of the liquid metal fiber composites; and (f) Junction distance illustration.

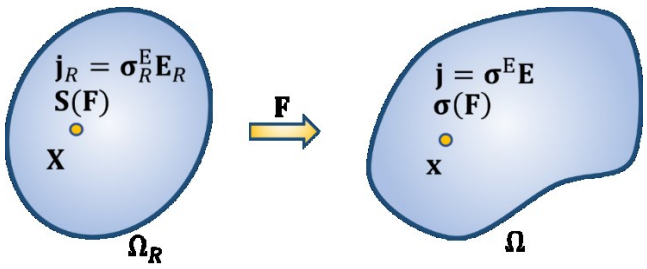

Figure 2. Continuum modeling of the electromechanical behavior of a soft conductor. The stress-strain relation and conductivity-strain relation can be formulated either in the reference configuration Ω_R or the current configuration Ω. There are two Ohm's laws considering the two configurations. Accordingly, we can define a material conductivity tensor $\boldsymbol{\sigma}_R^{\mathrm{E}}$ and a spatial conductivity tensor $\boldsymbol{\sigma}^{\mathrm{E}}$.

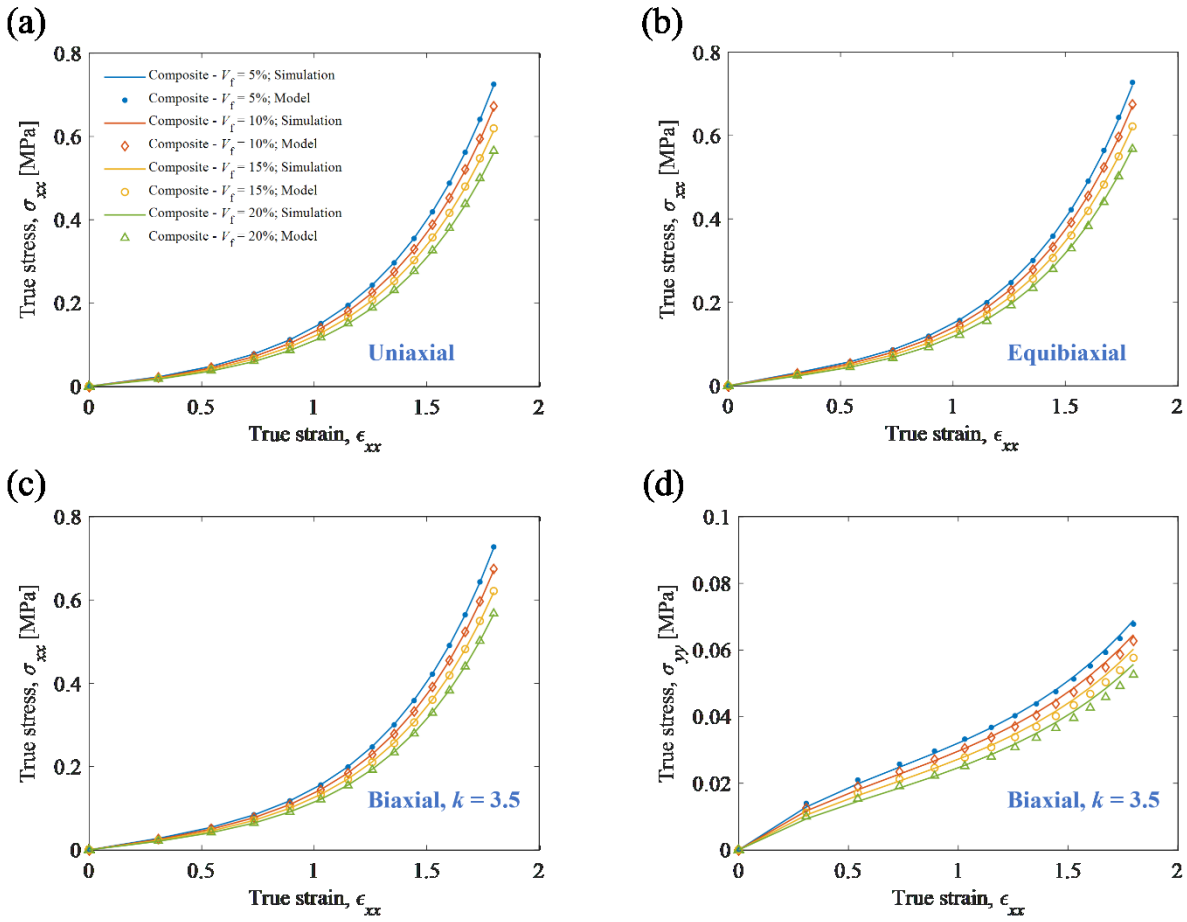

Figure 3. Stress-strain relations of the composites under different loading scenario: (a) Uniaxial loading, σ_{xx}; (b) Equibiaxial loading, $\sigma_{xx} = \sigma_{yy}$; (c) Biaxial loading, σ_{xx}; and (d) Biaxial loading, σ_{yy}.

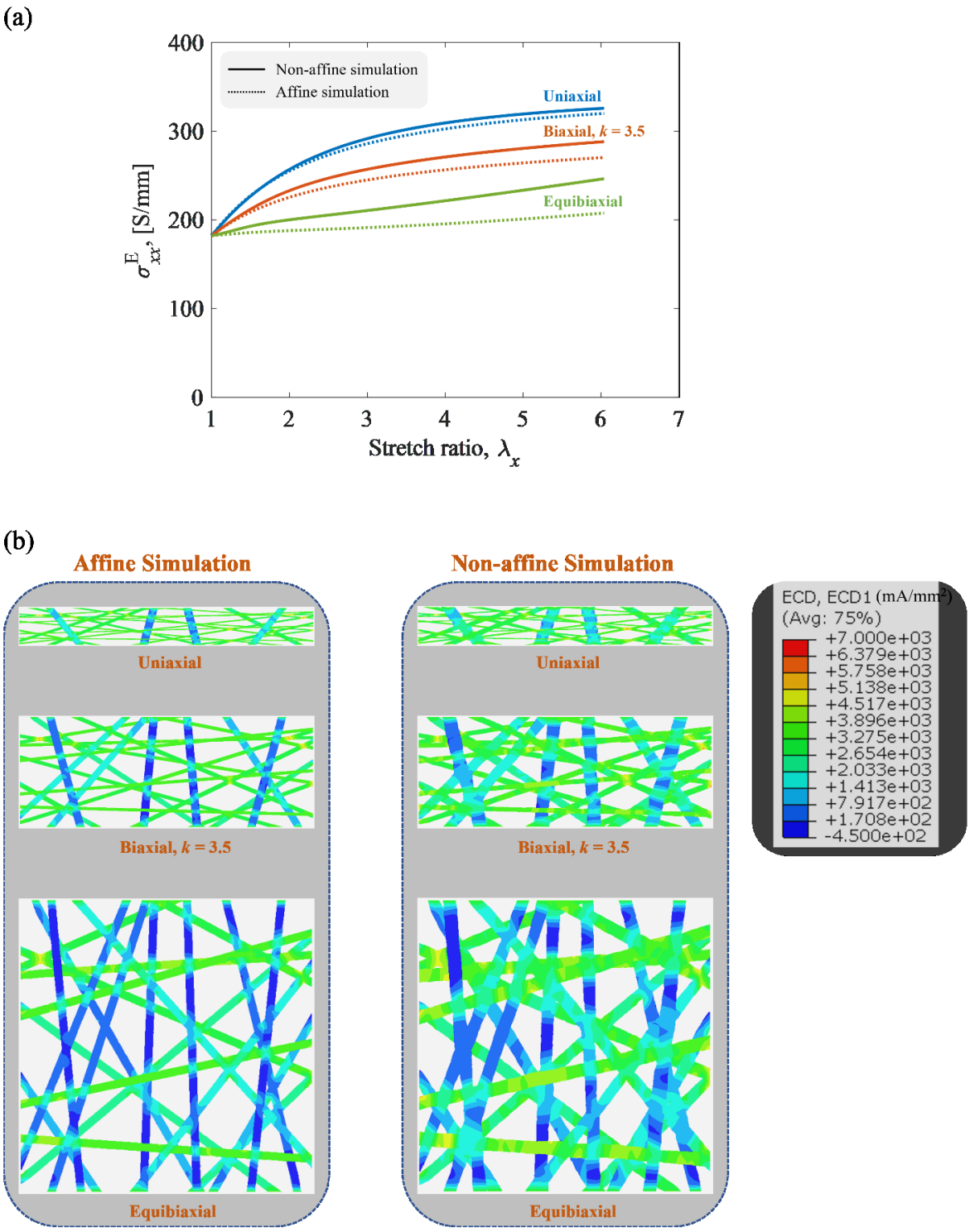

Figure 4. Conductivity-strain responses of the composite with affine and non-affine simulation for the case $V_f = 10\%$: (a) Spatial conductivity; (b) Electrical current density for $\lambda_x = 4$.

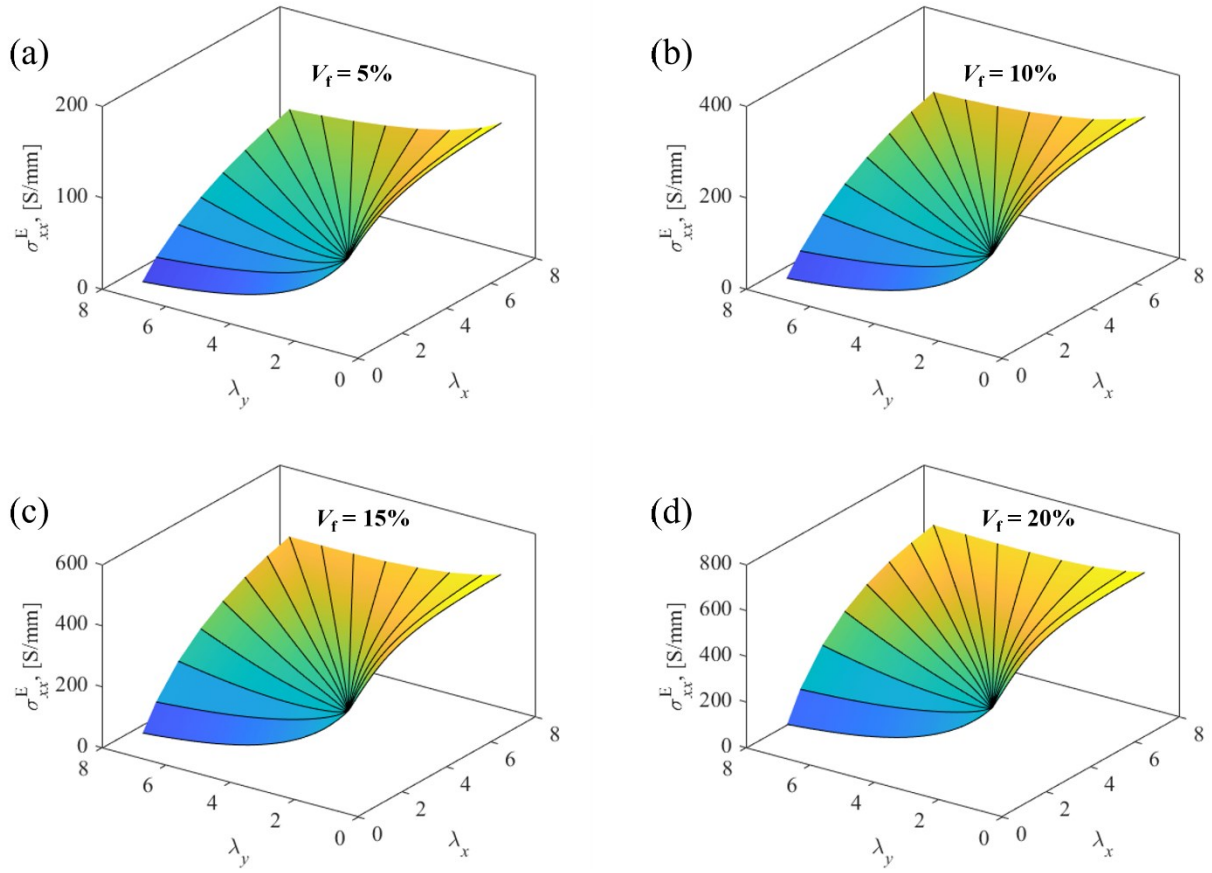

Figure 5. 3D surface plot of conductivity-strain relations under arbitrary biaxial loadings obtained from simulation: (a) $V_f = 5\%$; (b) $V_f = 10\%$; (c) $V_f = 15\%$; and (d) $V_f = 20\%$.

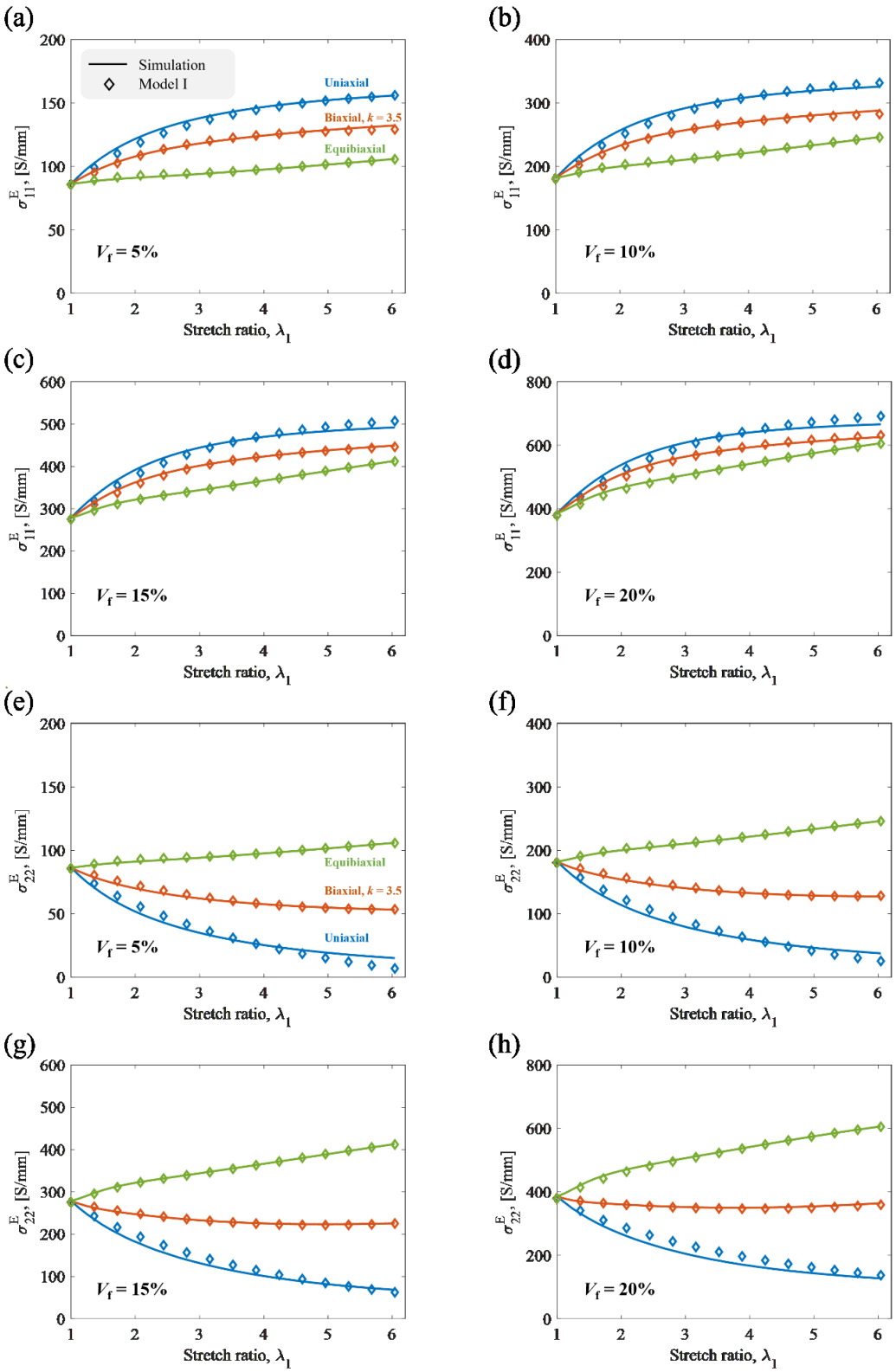

Figure 6. Conductivity-strain relations in the principal coordinate system from simulation and the conductivity model I. (a-d) σ_{11}^{E}; and (e-h) σ_{22}^{E}. The principal coordinate system is used here.

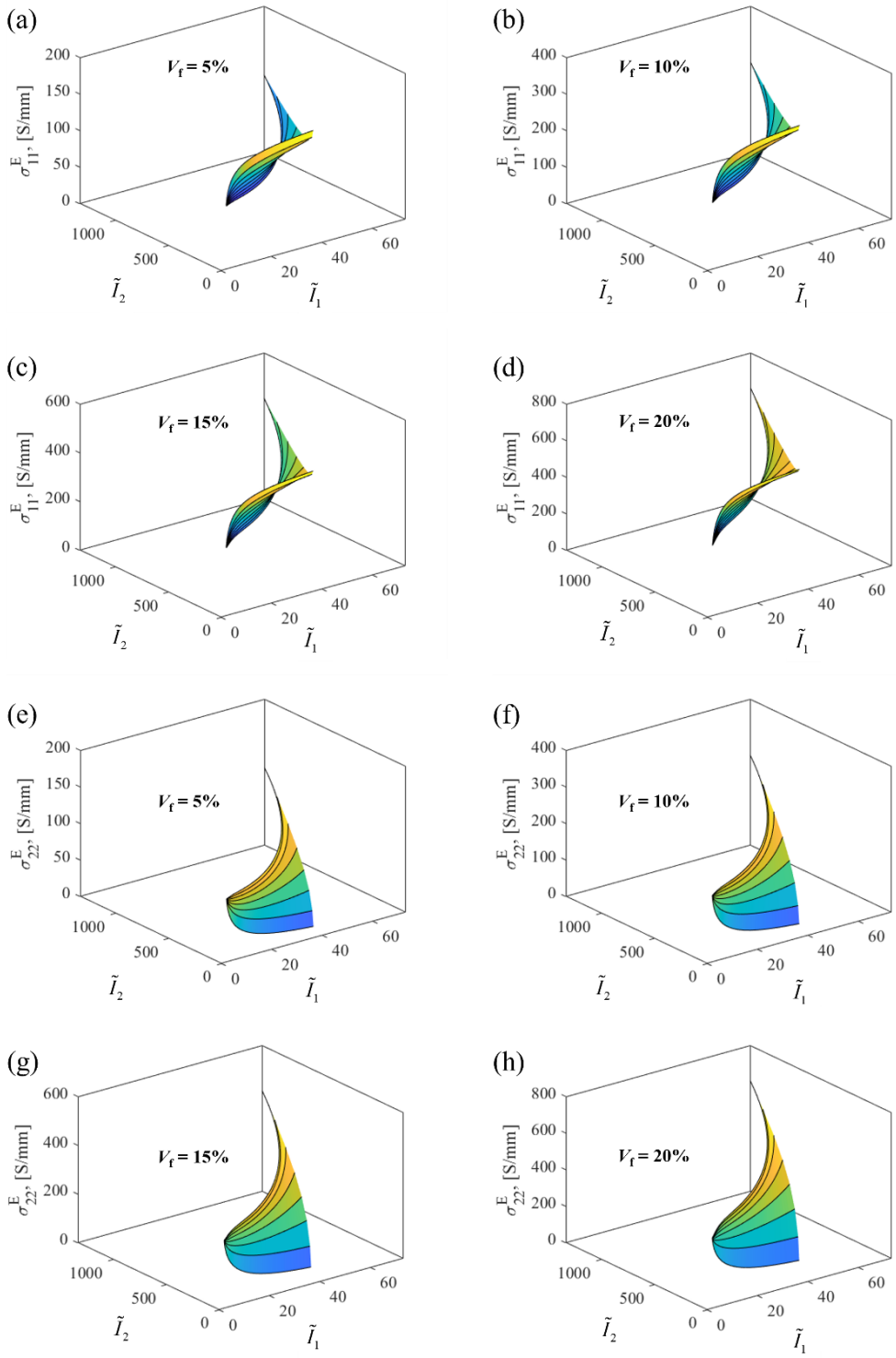

Figure 7. 3D surface plot of conductivity-strain relations in the invariant space under arbitrary biaxial loadings obtained from simulation: (a-d) σ^E_{11}; and (e-h) σ^E_{22}. The principal coordinate system is used here. The data are adapted from Figure 5.

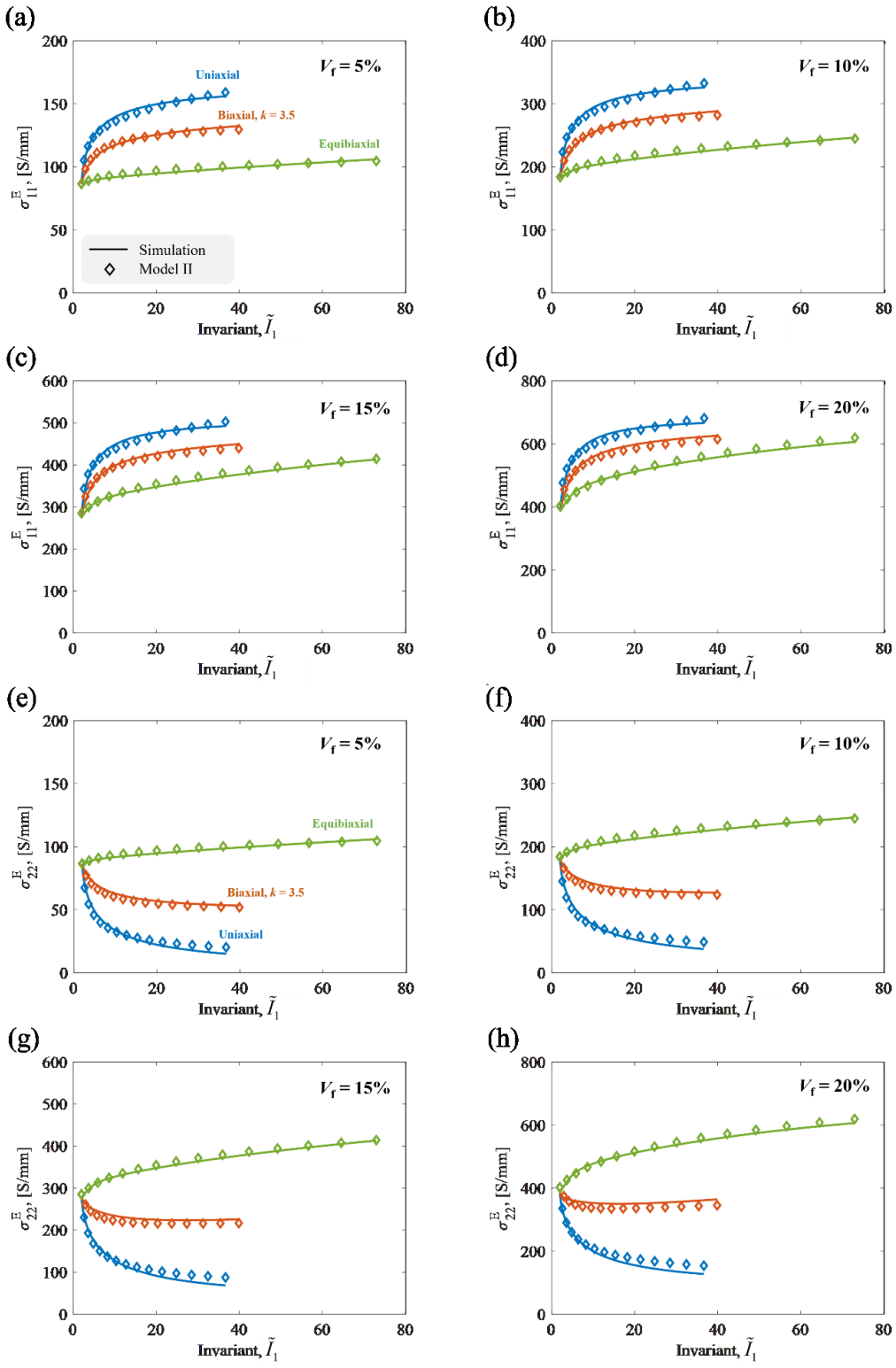

Figure 8. Conductivity-strain relations in the invariant space from simulation and the conductivity model II. (a-d) σ_{11}^E; and (e-h) σ_{22}^E.